A Sustainable and Tunable Mg/MgO Plasmon-Catalytic Platform for the Grand Challenge of SF_6 Environmental Remediation

Yael Gutiérrez,[1,2] Maria M. Giangregorio,[1] Fabio Palumbo,[1] Francisco González,[2] April S. Brown,[3] Fernando Moreno[1,2] and Maria Losurdo[1,§]*

[1]Institute of Nanotechnology, CNR-NANOTEC, via Amendola 122/D, 70126 Bari, Italy

[2]Optics Group, Department of Applied Physics, Faculty of Sciences, University of Cantabria, Avda. Los Castros s/n, 39005 Santander, Spain

[3] Department of Electrical and Computer Engineering, Duke University, Durham, 27708 NC, USA

Keywords: SF_6, magnesium, magnesium oxide, plasmonics, nanoparticles, plasmon-catalysis, environmental remediation

ABSTRACT

Sulfur hexafluoride (SF_6) is one of the most harmful greenhouse gases producing environmental risks. Therefore, developing ways of degrading SF_6 without forming hazard products is increasingly important.

Herein we demonstrate for the first time the plasmon-catalytic heterogeneous degradation of SF_6 into non-hazardous MgF_2 and $MgSO_4$ products by non-toxic and sustainable plasmonic magnesium/magnesium oxide (Mg/MgO) nanoparticles, which are also effective as a plasmon-enhanced SF_6 chemometric sensor. The main product depends on the excitation wavelength; when the localized surface plasmon resonance (LSPR) is in the ultraviolet then MgF_2 forms, while visible light LSPR results in $MgSO_4$. Furthermore, Mg/MgO platforms can be regenerated in few seconds by hydrogen plasma treatment and can be re-used in a new cycle of air purification. Therefore, this research first demonstrates effectiveness of Mg/MgO plasmon-catalysis enabling environmental remediation with the concurrent functionalities of monitoring, degrading and detecting sulfur- and fluorine- gases in the atmosphere.

1. Introduction

Sulfur hexafluoride (SF_6) is a long-lived highly potent greenhouse gas (GHG), with an atmospheric lifetime of 3200 years[1–3] and a global warming potential 24,000 times greater than CO_2[4,5] regulated under the Kyoto Protocol.[6] For those reasons, SF_6 was banned for its use in the European Union (EU) in 2014[7] with the exception of the electrical power industry, where SF_6 has been used as a dielectric and insulating material for many years in high-voltage circuit breakers, high-voltage transformers, distribution voltage switchgear, gas-insulated power substations, gas-insulated transmission lines, and radar equipment. All these applications release SF_6 into the atmosphere.[8] In its normal form, SF_6 is relatively harmless to humans. However, when exposed to electrical discharges typical for power applications, highly toxic by-products are produced, which include, among others, S_2F_{10}, considered by the US Environmental Protection Agency (EPA) "the by-product of greatest concern due to its relatively high toxicity."[9] Other by-products of SF_6 include thionyl sulphide (SOF_2), sulphur tetrafluoride (SF_4) and sulphuryl fluoride (SO_2F_2), with significant negative health impacts, including irritation to the eyes, nose and throat, pulmonary edema, skin and eye burns, nasal congestion and bronchitis.[10] Therefore, in 2014 the EU reinforced a 2006 fluorine-gas regulation,[7] aiming to reduce the EU's F-gas emissions in 2030 by two-third of the 2014 levels. This specific aim is part of the EU's ultimate objective of reducing by 2050 all GHG emissions by at least 80% of 1990 levels.[11]

Unlike CO_2, SF_6 has no effective disposal method, making its accumulation in the atmosphere irreversible. To date, SF_6 degradation has been achieved by combustion and plasma methods,[12] which, however, suffer from high energy consumption and release the toxic by-products mentioned above. Therefore, an eco-sustainable and efficient degradation technology for SF_6 gas that does not release hazardous by-products is urgently needed.

Magnesium (Mg) is gaining interest in recent years as an active element in a broad range of applications ranging from hydrogen storage[13] as magnesium hydride (MgH_2), to electronics as

the transparent semiconductor magnesium hydroxide ($Mg(OH)_2$)[14], and to plasmonics. Mg nanostructures support localized surface plasmon resonances (LSPR) tunable from the near-infrared (NIR) to the ultraviolet (UV)[15,16] suitable for sensing,[17] photovoltaic enhancement,[18] photocatalysis,[19] and photonic applications such as dynamic plasmonic color displays.[20] A Mg (metal)/MgO (dielectric) platform has recently been proposed for transient photonics.[21] Interestingly, the LSPR can also be exploited to promote chemical transformations, a phenomenon known as *plasmonic catalysis*, which has emerged as a novel frontier in nanocatalysis.[19,22,23] Additionally, nanoscale MgO structures, due to their high adsorption capacity, non-toxic nature, and limited solubility in water,[24] have emerged as appealing defluorination agent for the removal from water of fluoride, one of the major pollutants of groundwater.

Herein we demonstrate that the environmentally friendly, non-toxic, and sustainable magnesium/magnesium oxide (Mg/MgO) plasmonic nanoparticles (NPs) create an efficient plasmon-catalyst platform for the heterogeneous degradation of SF_6 to non-toxic products of MgF_2 and $MgSO_4$. Importantly, we demonstrate that the tunable LSPR of the Mg/MgO platform can be used to select the SF_6 degradation pathway and, therefore, the decomposition products: with LSPR in the ultraviolet photon energy range catalyzing the degradation to MgF_2 mainly, whereas LSPR in the visible range catalyzing mainly the SF_6 degradation pathway to $MgSO_4$. We also demonstrate that the plasmonic catalyst Mg/MgO NPs can be re-generated in a few seconds using a hydrogen plasma afterglow process at room temperature.

2. Results and Discussion

2.1 LSPR tunability, surface morphology and chemical analysis

We first demonstrate the tunability of the Mg NPs LSPR and its modification upon air exposure. Figure 1 shows the *real-time* evolution of the imaginary part of the pseudodielectric function, $\langle \epsilon_2 \rangle$, of two representative samples of Mg NPs recorded *in-situ* during their deposition on Al_2O_3. These spectra clearly show the appearance of LSPR peaks. Interestingly, as seen in Fig. 1(a,d), during the first 50 seconds of the deposition process, a LSPR peak appears at approximately 5.1 eV, which corresponds to Mg NPs with diameters smaller than 30 nm, consistent with observations of the LSPR of Mg NPs suitable for UV plasmonics.[15,16] With further Mg deposition, a LSPR peak at lower energies appear which red-shifts with increasing NP density, NPs size and cluster formation.[25] This provides evidence that by tailoring the size of self-assembled Mg NPs, a LSPR in the visible can be achieved. The histogram analysis of NP diameter (see Fig. 2), determined using AFM, corroborates these ellipsometric results showing that the 30 nm diameter NPs (Fig. 2(a)) evolve to NPs with a bimodal diameter distribution (Fig. 2(b,f)), explaining the appearance of a LSPR in the UV (generated by Mg NPs smaller than 30 nm in diameter) and a red-shifting LSPR generated by larger Mg NP clusters (50-100 nm).

Based on the LSPR energy, which results from the NPs size and therefore depends on the time of Mg deposition, we have grouped samples into two categories:

- (*UV*)Mg NPs: with LSPR peaks at energies above 3 eV (e.g. Fig. 1b),
- *(VIS-UV)*Mg NPs: with a LSPR extending into the visible range (e.g. Fig. 1e).

Figures 1(c,f) show the effect of a one day of air exposure on the LSPR of the two Mg NPs representative samples. A quenching of the plasmon resonance upon exposure to air is observed due to oxidation of the NPs, creating a shell of the dielectric oxide MgO around the Mg core,[16,25] as confirmed by XPS measurements (see Fig. 2(e,i)) and supported by electromagnetic simulations performed on a Mg/MgO core-shell sphere with total radius R = 50 nm, as shown in Fig. 1(h). Figure 1(i) shows a 2D color map of the spectral absorption efficiency (Q_{abs}) as a

function of the MgO shell thickness varied from 0 (100% Mg nanoparticle) to 50 nm (100% MgO nanoparticle). For small MgO thicknesses (< 10 nm), the excellent plasmon performance of Mg in the UV dominates[16] because the absorption of MgO is negligible in this spectral range. The Mg plasmon performance reduces with the increase in the MgO shell to the point at which the plasmon peak is fully quenched. Despite this effect on the LSPR amplitude, the MgO shell plays an important role in the electron transfer (ET), via electron tunneling, from the plasmonic Mg core to adsorbed SF_6 molecules as explained in the below (see Fig. 3(a)). Full quenching of the plasmon resonance upon further exposure of the same samples to air contaminated with SF_6 is observed (Fig. 1(c,f)).

Figure 2(b,f) shows the different change in the surface morphology of the Mg NPs samples in Fig. 1 after one day exposure to an atmosphere contaminated by SF_6. Upon exposure to SF_6 contaminated air, micron-size dendritic crystals of different shape and density form depending on the Mg/MgO LSPR energy. The color contrast in the phase images indicates that these crystals are of a different chemical nature than the Mg/MgO nanoparticles. The composition of those crystals has been determined by combining Raman spectra, FTIR absorbance spectra and XPS Mg2*p*, O1*s*, F1*s* and S2*p* photoelectron core level spectra reported in Fig. 2. The details of those analyses reported in SI confirm different chemical transformations and indicate different pathways of SF_6 decomposition on the Mg/MgO surface depending on the energy (wavelength) of the LSPR. Specifically, the *(UV)*Mg NPs decompose SF_6 to MgF_2 mainly, while the *(VIS-UV)*Mg NPs sample results in $MgSO_4$ as main product.

2.2 Plasmon-selective SF_6 degradation pathways

According to the above findings and analyses, different SF_6 degradation pathways are proposed as shown in Fig. 3(b,c). SF_6 decomposition into SF_5 and fluorine radicals requires 4.04 ± 0.14 eV

(bond dissociation energy); achieving this energy is difficult without UV illumination, and photodissociation is achieved when the photon energy exceeds ~10 eV,[26] or by electrons with energy > 4 eV.

Here, considering the energy diagram in Fig. 3(a), the work function, W_F, of Mg = 3.7 eV, and the energy levels of the MgO valence band and conduction band, the latter almost resonant with the SF_6 electron affinity level, we take advantage of the LSPR at approximately 5 eV yielding free electrons that can be transferred through MgO to SF_6 molecule, which is a well-known electron-scavenger molecule, i.e., attachment of free electrons to SF_6 has a very low activation energy of 0.2-0.4 eV.[27] The dissociative electron attachment of SF_6 is also well known and very fast; hence, SF_6 directly adsorbs on the Mg/MgO surface, it captures electrons with one of the highest cross sections[28] and dissociate into SF_5 and F-radicals according to the reaction

$$SF_6 + e \rightarrow \cdot SF_5 + F^- \quad (1)$$

This heterogeneous dissociation of SF_6 is consistent with the absence of any SF_6 signal in the XPS, FTIR and Raman spectra.

As shown in Fig. 3(b), the subsequent steps of SF_5 heterogeneous dissociation require electrons with energy > 4 eV that are activated by the light exciting the LSPR in the UV, generating hot electrons with nearly free-electron behavior. This leads to cascade dissociation channels as shown below:

$$SF_5 + e(>4.5eV) \rightarrow \underset{+F}{SF_4} \rightarrow \underset{+F}{SF_3} \rightarrow \underset{+F}{SF_2} \rightarrow \underset{+F}{SF} \rightarrow S \quad (2)$$

The fluorine reacting at the Mg/MgO surface results mainly in MgF_2 and MgO_xF_y, and a relatively small amount of $MgSO_4$ as observed for the (*UV*)Mg NPs sample.

On the other hand, the LSPR at approximately 1.5 - 2 eV is resonant with the following dissociation channels yielding primarily adsorbed SO_2:

$\cdot SF_5 + e^- (1.6\ eV) \rightarrow \cdot SF_4 + F^-$

$\cdot SF_3 + e^- (2\ eV) \rightarrow \cdot SF_2 + F^-$

with the $\cdot SF_4$ and $\cdot SF_2$ radicals reacting with moisture and oxygen and/or the O-sites and OH-sites of MgO according to the reaction:

$$SF_2 \xrightarrow{O/OH/H_2O} SOF_2 \xrightarrow{H_2O} SO_2 + 2HF \quad (3)$$

As a result, the formation of $MgSO_4$ can be explained in two steps. First, the heterogeneous reaction of adsorbed SO_2 on acidic magnesium sites (Mg^{2+}) of MgO forming $MgSO_3$

$$MgO + SO_2 \rightarrow MgSO_3 \quad (4)$$

This reaction has already been observed by Czyżewski et al. on MgO loaded porous carbons.[29] Second, the further oxidation of $MgSO_3$ leads to $MgSO_4$, as reported by Luque et al.[30] and occurs in the presence of humid air through the reaction

$$MgSO_3 + ½\ O_2 + 7\ H_2O \rightarrow MgSO_4 \bullet 7\ H_2O \quad (5)$$

It has been suggested by the theoretical study of Pacchioni et al.[31] that sulfate can also form heterogeneously by interaction of the sulfur atom in sulfite with two oxide anions on the unreconstructed MgO surface.

On the other hand, oxyfluorides may arise from the reaction of hydrogen fluoride (HF) from reaction (3) with MgO, i.e.,

$$MgO + 2\ HF \rightarrow MgF_2 + H_2O \quad (6)$$

$$MgO + x\ HF \rightarrow MgO_{1-x/2}F_x + x/2\ H_2O \quad (7)$$

$$MgO + CH_xF_{4-x} \rightarrow MgOF_{4-x} + x/4\ CH_4 \quad (8)$$

Therefore, the wavelength-dependence of the observed products demonstrates that the LSPR of Mg/MgO NPs produces the heterogeneous decomposition of SF_6 to primarilyMgF_2 or $MgSO_4$, both non-toxic products.

2.3 Differentiating thermal versus non-thermal plasmon-catalytic effects

In plasmon-catalysis, the distinction between thermal and non-thermal contributions is challenging and controversial.[22,32] Therefore, we have performed several tests to prove our plasmonic catalytic effects:

- Both Mg-face and the O-face MgO(111) single crystals with very rough surfaces and, therefore, a high surface area for adsorption (roughness peak-to-valley, $R_{p-v} \sim 20$ nm, comparable to that measured for the used NPs samples), as well as polycrystalline 2 mm thick disks of magnesium, have been exposed for 60h to the same SF_6 contaminated atmosphere, maintaining them at a controlled temperature in the range 25 - 600°C. In this case, in absence of LSPR, up to a temperature of 500°C only oxidation of the samples has been observed, consistent with the high thermal stability of SF_6.[33] This provides indication that the LSPR is needed to catalyze SF_6 decomposition.
- In order to verify the wavelength-dependent plasmonic effect, samples of Mg/MgO with LSPR at 1.9 eV, at 2.5 eV and at 4.7 eV have been exposed to the same SF_6 contaminated atmosphere and concurrently irradiated with off-resonant and resonant lasers with wavelengths of 787 nm (1.57 eV), 633 nm (1.95 eV), 532 nm (2.33 eV) and 473 nm (2.62 eV) (laser power 5 mW) for 30min. The sample with LSPR at 4.7 eV has been irradiated with an UV-lamp (deuterium lamp, 160 - 400 nm (3.1 - 7.75 eV)) for 30 min. The samples were mounted in a temperature-programmable and controllable cell and monitored by Raman spectroscopy. The results are reported in Fig. 3(d). For each sample we measured the

Raman spectra after irradiation with different wavelength light, specifically monitoring the primary -products of $MgSO_4$ at 986 cm^{-1} and MgF_2 at 469 cm^{-1}. The intensity of these product signals is a measure of the SF_6 decomposition efficiency enabled by the different laser irradiation wavelengths. Since the laser irradiation at 787 nm is off resonance for all samples, the Raman spectrum did not show any relevant peak due to SF_6 products, indicating that no plasmon-catalyzed decomposition occurred. The maximum intensity signal for the peak at 986 cm^{-1} of $MgSO_4$ was obtained for the resonance irradiation condition of 633 nm for the sample with the LSPR at 1.9 eV; a maximum intensity for the MgF_2 peak at 469 cm^{-1} was obtained for the resonance condition of 532 nm irradiation for the sample with the LSPR at 2.5 eV and with the UV lamp irradiation of the sample with LSPR at 4.7 eV. The observed wavelength-dependent products formation supports the plasmon-catalytic effect.

2.4 Regeneration of Mg/MgO NPs platform

Interestingly, we found that the Mg/MgO NP platforms can be regenerated and reused in a new SF_6 degradation cycle by removing MgF_2/MgO_xF_y and $MgSO_4$ products from the sample surface. The regeneration of the Mg/MgO is performed by exposing it to a remote hydrogen plasma at a temperature of <100ºC for few seconds (the specific time being dependent on the size of the Mg/MgO sample to regenerate and on the plasma parameters) as shown in Fig. 4(a,b); the micrographs and the XPS survey spectra of the sample before and after the hydrogen show disappearing of S2p and F1s signals, while Fig. 4(c) shows the faster kinetics of its re-use (for details see SI).

2.5 Plasmonic and Colorimetric Sensing of SF_6 photocatalysis

The plasmon-catalyzed degradation of SF_6 entails a change in the pseudodielectric function of the Mg/MgO NPs platform, with the LSPR of the Mg/MgO NPs being quenched and blue-shifted due to the LSPRs sensitivity to changes in the refractive index from MgO to $MgSO_4$ and MgF_2. This phenomenon opens the possibility of using either the spectroscopy of LSPRs or colorimetry measurements of the Mg/MgO NPs samples to detect and monitor the products from the photocatalyzed transformation of the MgO-shell/Mg-core nanoparticles into $MgSO_4$ and MgF_2. To demonstrate this, we have performed electromagnetic simulations on a Mg/MgO core-shell spherical nanoparticle (total radius R = 50 nm and core radius $R_c \in [0, 25]$ nm) with the MgO shell being converted progressively into $MgSO_4/MgF_2$ until MgO is completely transformed (100% $MgSO_4/MgF_2$ shell) (see inset in 5(c)). Figures 5(b) and 5(c) plots the spectral shift ($\Delta\lambda$) of the LSP dipolar resonance as the MgO shell is converted to $MgSO_4/MgF_2$ with respect to the spectral position of the 100% MgO shell. This calculation has been performed for different values of R_c while keeping the total R = 50 nm. In both cases, the transformation of the MgO shell into $MgSO_4/MgF_2$ produces a blue-shift of the LSPR, consistent with the experimental results in Fig.1(c,f). This can be rationalized by considering the refractive index of $MgSO_4$ and MgF_2, n, lower than MgO (the latter being 1.73[34] *vs* 1.54[35] for $MgSO_4$ and 1.42[36] for MgF_2); consequently, as the thickness of the $MgSO_4/MgF_2$ layer increases, the refractive index of the effective surrounding medium of the Mg core lowers, leading to a blue-shift of the LSPR. Since the contrast between the refractive indices of MgO and MgF_2 is higher than that of MgO and $MgSO_4$, the blue shift for MgF_2 formation is larger than for $MgSO_4$. In both cases, the sensitivity of the LSPR to the formation of a very thin shells of $MgSO_4(MgF_2)$ increases with R_c. For instance, for the highest (25 nm) and lowest (5 nm) values of R_c considered, the values of $\Delta\lambda$ for a $MgSO_4$ (MgF_2) shell thickness of 5 nm are -2.3 and 0 (-3.6 and 0 nm), respectively. Therefore, the sensitivity to the conversion of the MgO shell into $MgSO_4/MgF_2$ increases with

the amount of metallic Mg in the NPs (larger values of R_c). This can be understood considering the change in the refractive index experienced by the near-field around the Mg core. Figure 5(b) maps the modulus of the near electric field |**E**| for Mg/MgO/MgF_2 multilayered spheres with R_c = 5 and 25 nm, and a MgF_2 shell of 5 nm. Note that the maps for the Mg/MgO/$MgSO_4$ (not shown here) are very similar. For the smallest cores and the thinner $MgSO_4$/MgF_2 shells, the range of the near field, which decays with the square of the distance, does not reach the boundary between the MgO and $MgSO_4$/MgF_2, being its response insensitive to the growing shell (see Fig. 5(b) bottom). However, in NPs with higher values of R_c, the near-field range produced by the Mg core reaches the boundary between MgO and $MgSO_4$/MgF_2, consequently, even for the thinner shells, a blue-shift of the LSPR is experienced (see Fig. 5(b) top). From a practical point of view, these results provide a guidance to design the appropriate NPs size for exploiting the sensing to the photocatalytic effect.

Furthermore, this feature may allow detecting or even monitoring the evolution of $MgSO_4$/MgF_2 formation on Mg/MgO surfaces using colorimetric measurements. In order to study the change of color in our samples we have performed colorimetric simulations in multilayer systems as in Fig. 5(d), consisting of: (i) an infinite Al_2O_3 substrate, (ii) a Mg layer of thickness h, (iii) a layer of MgO which is converted to $MgSO_4$/MgF_2 and (iv) air as surrounding medium. The total thickness of the Mg and MgO layers has been fixed to 50 nm. We have calculated the color coordinates, L^*a^*b, for Mg layer thicknesses, h, ranging between 5 and 20 nm. These values have been chosen to be consistent with our samples in Fig. 1. Each point in the Figs. 6(e-g) corresponds to increasing thickness of the $MgSO_4$/MgF_2 layer that ultimately consumes the MgO. The sweep goes from 100% MgO to 100% $MgSO_4$(or MgF_2) in steps of 1 nm. The color of each dot corresponds to the color of the film. As the value of h increases (more Mg in the system), the value of the luminosity L^* increases, leading to a shinier appearance more

characteristic of metallic surfaces. The samples have a brownish color that becomes lighter as *h* increases. In order to objectively evaluate how the color of the system changes as the thickness of $MgSO_4/MgF_2$ layer increases with respect to MgO layer, we have calculated the value of ΔE between these two situations for different values of *h* as a function of the thickness of the $MgSO_4/MgF_2$ layer (see Figs. 6(h,i)). The color difference between two points in the *L*a*b** space is defined as $\Delta E = \sqrt{(a_1^* - a_2^*)^2 + (b_1^* - b_2^*)^2 + (L_1^* - L_2^*)^2}$. In our case $L_1{*}a_1{*}b_1{*}$ corresponds to the color coordinates of the system with 100% MgO layer and $L_2{*}a_2{*}b_2{*}$ corresponds to the color coordinates of the system with different thicknesses of the $MgSO_4/MgF_2$ layers. A growing MgF_2 layer yields values of ΔE higher than $MgSO_4$ because of the higher contrast in the refractive index between MgO and MgF_2 than $MgSO_4$. In light of these results, the measurement of ΔE can be used to detect and monitor the by-products grown on the surface of Mg/MgO NPs coming from the plasmon-catalyzed decomposition of SF_6.

3. Conclusions

The non-toxic and sustainable plasmonic Mg/MgO nanoparticles platform has been proven to plasmon-catalyze the heterogeneous degradation of the long-lived greenhouse gas SF_6 into non-hazardous MgF_2 and $MgSO_4$ products and to effectively capture those them. Moreover, surface plasmon resonance of those nanoparticles can be used to tune the main product, being MgF_2 produced with a plasmonic resonance in the UV range, and $MgSO_4$ produced when the plasmon resonance is in the VIS range. Mg/MgO platforms can be regenerated using a hydrogen plasma treatment at T < 100ºC that reduces the contaminants in the sample, so that it can be used in a new cycle of air purification. Furthermore, the plasmonic Mg/MgO NPs platform functions also as plasmon-enhanced colorimetric sensor to SF_6 degradation.

Therefore, this research identifies a new application of plasmon catalysis for environmental remediation by demonstrating that Mg/MgO NP platforms function air purifiers that absorb, monitor and detect the presence of SF_6 in air.

Supplementary Information

Detailed chemical analysis of the samples; chemical analysis of the samples after H-plasma treatment; experimental details.

Acknowledgements

Y.G., F.G. and F.M. acknowledge MICINN (Spanish Ministry of Science and Innovation) through project PGC2018-096649-B-100. Y.G. thanks the University of Cantabria for her FPU grant.

Corresponding Authors

E-mail: * yael.gutierrezvela@unican.es and § maria.losurdo@cnr.it

Conflict of Interest

The authors declare no conflict of interests

References

(1) Diggelmann, Thomas Tehlar, D.; Chang, J.; Zache, S. An Alternative to SF6 in Electrical Switchgear. *ABB Rev.* **2016**. https://library.e.abb.com/public/3405a31190934a8c98997eca8fc811be/ABB%20Review%202-2016_AirPlus_An%20Alternative%20to%20SF6.pdf (accessed 2020-03-25)

(2) Blackman, J.; Kantamaneni, R. Global Mitigation of Non-CO2 Greenhouse Gases: 2010-2030. *U.S. Environ. Prot. Agency (U.S. EPA)* **2013**, No. EPA-430-R-13-011.

(3) Dervos, C. T.; Vassiliou, P. Sulfur Hexafluoride (SF 6): Global Environmental Effects and Toxic Byproduct Formation. *J. Air Waste Manage. Assoc.* **2000**, *50* (1), 137–141.

(4) Fang, X.; Hu, X.; Janssens-Maenhout, G.; Wu, J.; Han, J.; Su, S.; Zhang, J.; Hu, J. Sulfur Hexafluoride (SF 6) Emission Estimates for China: An Inventory for 1990–2010 and a Projection to 2020. *Environ. Sci. Technol.* **2013**, *47* (8), 3848–3855.

(5) Blackburn, L. S. WHITE PAPER: SF6 Is No Longer a Necessary Evil: The Human Health and Environmental Dangers of SF6 Gas-Filled Switchgear. *Innov. Switchg. Solut. Inc.* **2015**.

(6) Rigby, M.; Mühle, J.; Miller, B. R.; Prinn, R. G.; Krummel, P. B.; Steele, L. P.; Fraser, P. J.; Salameh, P. K.; Harth, C. M.; Weiss, R. F.; et al. History of Atmospheric SF 6 from 1973 to 2008. *Atmos. Chem. Phys.* **2010**, *10* (21), 10305–10320.

(7) European Union Commisssion. *EU Legislation to Control F-Gases*. https://ec.europa.eu/clima/policies/f-gas/legislation_en (access 2020-03-25)

(8) *Gaseous Dielectrics X*; Christophorou, L. G., Olthoff, J. K., Vassiliou, P., Eds.; Springer US: Boston, MA, 2004.

(9) ICF Consulting. Byproducts of Sulfur Hexafluoride (SF6) Use in the Electric Power Industry. *U.S. Environ. Prot. Agency (U.S. EPA)* **2002**.

(10) Tsai, W.-T. The Decomposition Products of Sulfur Hexafluoride (SF6): Reviews of Environmental and Health Risk Analysis. *J. Fluor. Chem.* **2007**, *128* (11), 1345–1352.

(11) European Union Commisssion. *Climate strategies & targets; 2050 long term strategy*. https://ec.europa.eu/clima/policies/strategies/2050_en (access 2020-03-31)

(12) Radoiu, M.; Hussain, S. Microwave Plasma Removal of Sulphur Hexafluoride. *J. Hazard. Mater.* **2009**, *164* (1), 39–45.

(13) Zhu, M.; Lu, Y.; Ouyang, L.; Wang, H. Thermodynamic Tuning of Mg-Based Hydrogen Storage Alloys: A Review. *Materials (Basel).* **2013**, *6* (10), 4654–4674.

(14) Karazhanov, S. Z.; Pishtshev, A.; Klopov, M. Electronic and Optical Properties of Magnesium and Calcium Hydroxides: The Role of Covalency and Many-Body Effects. *Phys. Scr.* **2015**, *90* (9), 094015.

(15) Gutiérrez, Y.; Alcaraz, R.; Osa, D.; Ortiz, D.; Saiz, J. M.; González, F.; Moreno, F. Plasmonics in the Ultraviolet with Aluminum, Gallium, Magnesium and Rhodium. *Appl. Sci.* **2018**, *8* (1), 64.

(16) Sanz, J. M.; Ortiz, D.; Alcaraz de la Osa, R.; Saiz, J. M.; González, F.; Brown, a. S.; Losurdo, M.; Everitt, H. O.; Moreno, F. UV Plasmonic Behavior of Various Metal Nanoparticles in the Near- and Far-Field Regimes: Geometry and Substrate Effects. *J. Phys. Chem. C* **2013**, *117* (38), 19606–19615.

(17) Sharma, B.; Frontiera, R. R.; Henry, A.-I.; Ringe, E.; Van Duyne, R. P. SERS: Materials, Applications, and the Future. *Mater. Today* **2012**, *15* (1–2), 16–25.

(18) Atwater, H. A.; Polman, A. Plasmonics for Improved Photovoltaic Devices. *Nat. Mater.* **2010**, *9* (3), 205–213.

(19) Kale, M. J.; Avanesian, T.; Christopher, P. Direct Photocatalysis by Plasmonic Nanostructures. *ACS Catal.* **2014**, *4* (1), 116–128.

(20) Duan, X.; Liu, N. Scanning Plasmonic Color Display. *ACS Nano* **2018**, *12* (8), 8817–8823.

(21) Farinha, T. G.; Gong, C.; Benson, Z. A.; Leite, M. S. Magnesium for Transient Photonics. *ACS Photonics* **2019**, *6* (2), 272–278.

(22) Zhang, X.; Li, X.; Reish, M. E.; Zhang, D.; Su, N. Q.; Gutiérrez, Y.; Moreno, F.; Yang, W.; Everitt, H. O.; Liu, J. Plasmon-Enhanced Catalysis: Distinguishing Thermal and Nonthermal Effects. *Nano Lett.* **2018**, *18* (3), 1714–1723.

(23) Aslam, U.; Rao, V. G.; Chavez, S.; Linic, S. Catalytic Conversion of Solar to Chemical Energy on Plasmonic Metal Nanostructures. *Nat. Catal.* **2018**, *1* (9), 656–665.

(24) Wang, L. C.; Ge, Q. F. Studies of Rhodium Nanoparticles Using the First Principles Density Functional Theory Calculations. *Chem. Phys. Lett.* **2002**, *366*, 368–376.

(25) Gutiérrez, Y.; Giangregorio, M. M.; Palumbo, F.; Brown, A. S.; Moreno, F.; Losurdo, M. Optically Addressing Interaction of Mg / MgO Plasmonic Systems with Hydrogen. *Opt. Express* **2019**, *27* (4), A197–A205.

(26) Babcock, L. M.; Streit, G. E. Negative Ion–Molecule Reactions of SF 4. *J. Chem. Phys.* **1981**, *75* (8), 3864–3870.

(27) Matejcik, S.; Eichberger, P.; Plunger, B.; Kiendler, A.; Stamatovic, A.; Märk, T. D.

Dissociative Electron Attachment to SF6: Production of SF5− at Temperatures below 300 K. *Int. J. Mass Spectrom. Ion Process.* **1995**, *144* (3), L13–L17.

(28) Christophorou, L. G.; Olthoff, J. K. Electron Interactions With SF6. *J. Phys. Chem. Ref. Data* **2000**, *29* (3), 267–330.

(29) Czyżewski, A.; Kapica, J.; Moszyński, D.; Pietrzak, R.; Przepiórski, J. On Competitive Uptake of SO2 and CO2 from Air by Porous Carbon Containing CaO and MgO. *Chem. Eng. J.* **2013**, *226* (5), 348–356.

(30) Luque, A.; Martínez de Yuso, M. V.; Cultrone, G.; Sebastián, E. Analysis of the Surface of Different Marbles by X-Ray Photoelectron Spectroscopy (XPS) to Evaluate Decay by SO2 Attack. *Environ. Earth Sci.* **2013**, *68* (3), 833–845.

(31) Pacchioni, G.; Clotet, A.; Ricart, J. M. A Theoretical Study of the Adsorption and Reaction of SO2 at Surface and Step Sites of the MgO(100) Surface. *Surf. Sci.* **1994**, *315* (3), 337–350.

(32) Jain, P. K. Taking the Heat Off of Plasmonic Chemistry. *J. Phys. Chem. C* **2019**, *123* (40), 24347–24351.

(33) Zeng, F.; Tang, J.; Fan, Q.; Pan, J.; Zhang, X.; Yao, Q.; He, J. Decomposition Characteristics of SF 6 under Thermal Fault for Temperatures below 400°C. *IEEE Trans. Dielectr. Electr. Insul.* **2014**, *21* (3), 995–1004.

(34) Palik, E. D. *Handbook of Optical Constants of Solids*; Academic Press, 1998.

(35) Haynes, W. M. *CRC Handbook of Chemistry and Physics*, 95th ed.; Taylor and Francis Group, LLC, 2014.

(36) Rodríguez-de Marcos, L. V.; Larruquert, J. I.; Méndez, J. A.; Aznárez, J. A. Self-Consistent Optical Constants of MgF_2, LaF_3, and CeF_3 Films. *Opt. Mater. Express* **2017**, *7* (3), 989.

TOC FIGURE

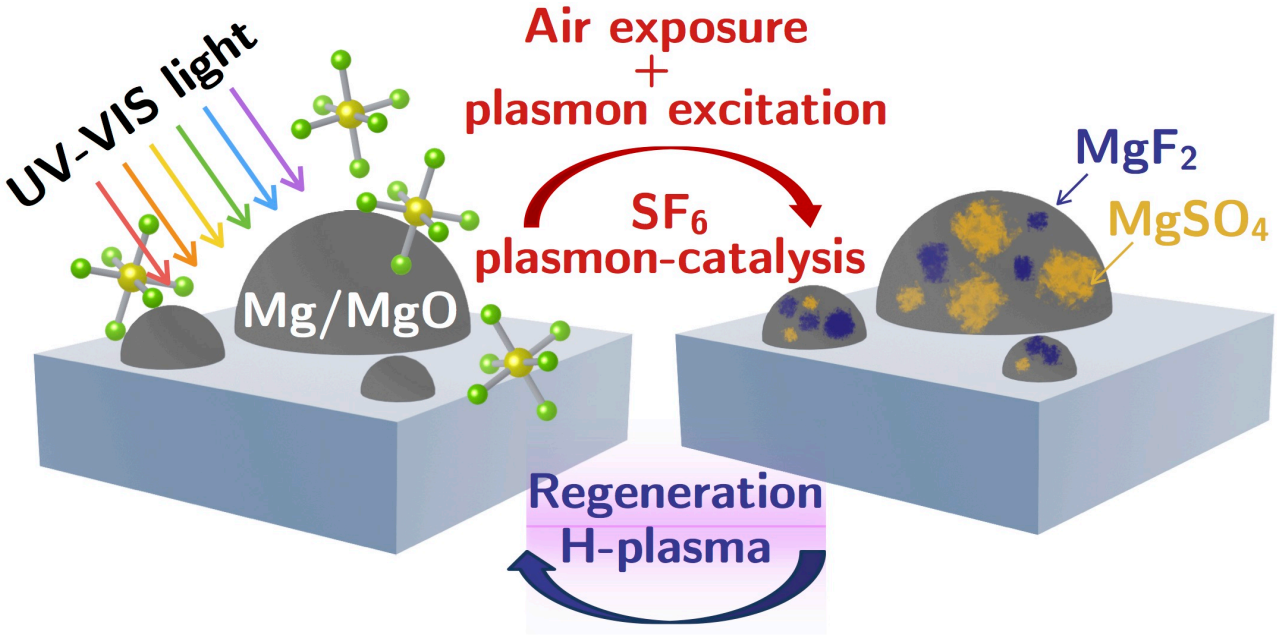
UV-VIS light
Air exposure
+
plasmon excitation
SF6
plasmon-catalysis
Mg/MgO
MgF2
MgSO4
Regeneration
H-plasma

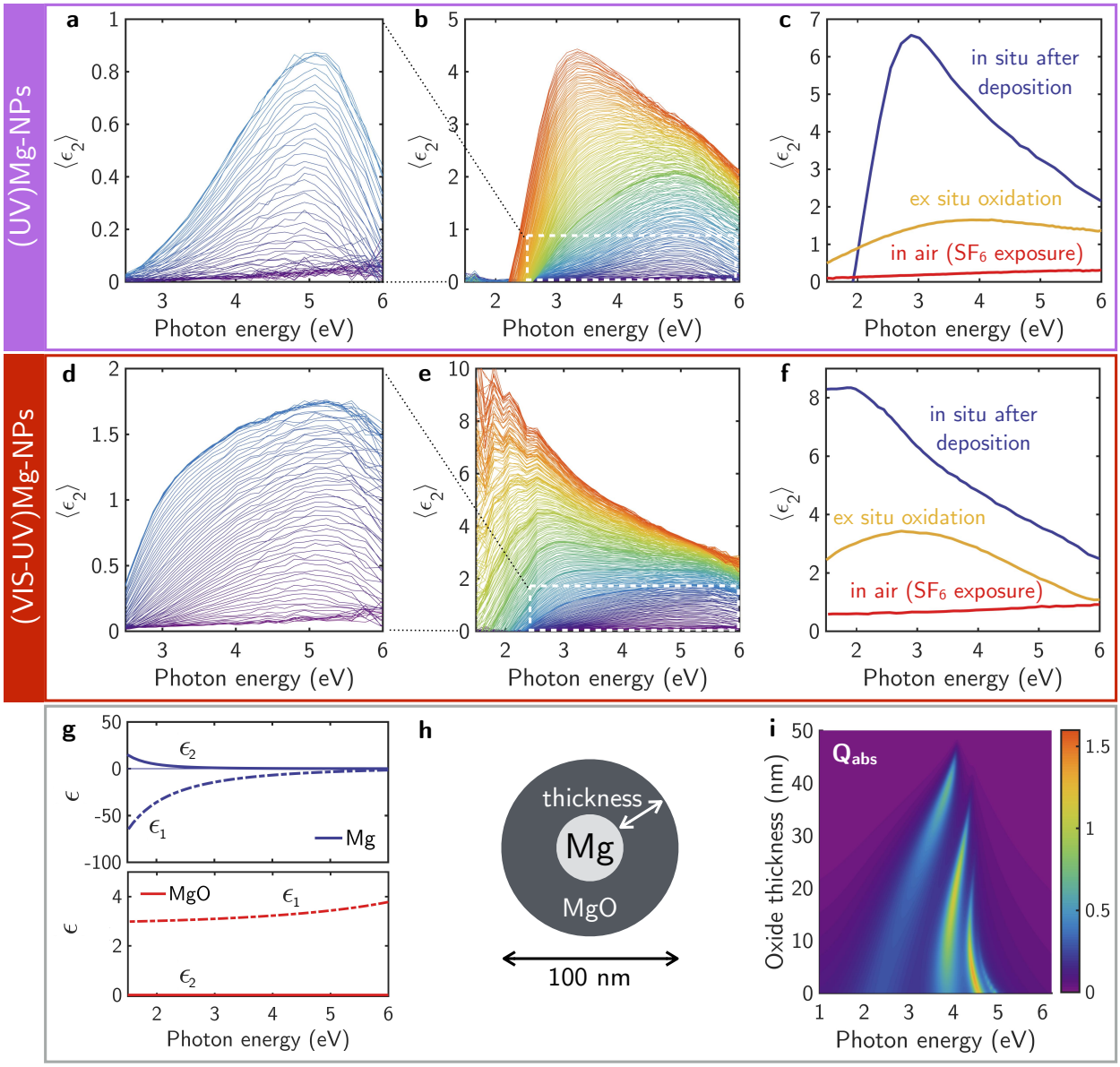

Figure 1. **Real-time evolution of the imaginary part, <ε₂>, of the pseudodielectric function showing the localized surface plasmon resonance peak monitored by spectroscopic ellipsometry during the nucleation and growth of Mg NPs and its subsequent exposure to air and to SF_6 contaminated air**. (**a, d)** Real-time evolution of the Mg NPs plasmon resonance during**,** the first 50 seconds (a) and 70 sec (d) of Mg deposition; each ellipsometric spectrum is taken every 1 sec. **(b, e)** show the further evolution of the plasmon resonance red-shifting with increasing the Mg deposition time to 200 sec (b) and 400 sec (**e**); each spectrum is taken every 1

sec. **(c, f)** Ellipsometric spectra of the imaginary part, $\langle \varepsilon_2 \rangle$, of the pseudodielectric function showing the plasmon resonance spectra evolution during exposure to SF_6 contaminated air. **(g)** Complex dielectric function $\epsilon = \epsilon_1 + i\epsilon_2$ of Mg and MgO. **, (h)** Scheme of the geometry of Mg/MgO core-shell spherical NP of total radius R = 50 nm used for electromagnetic simulations. (**i**) 2D color map of the spectral absorption efficiency (Q_{abs}) of a Mg/MgO core-shell as a function of the MgO shell thickness.

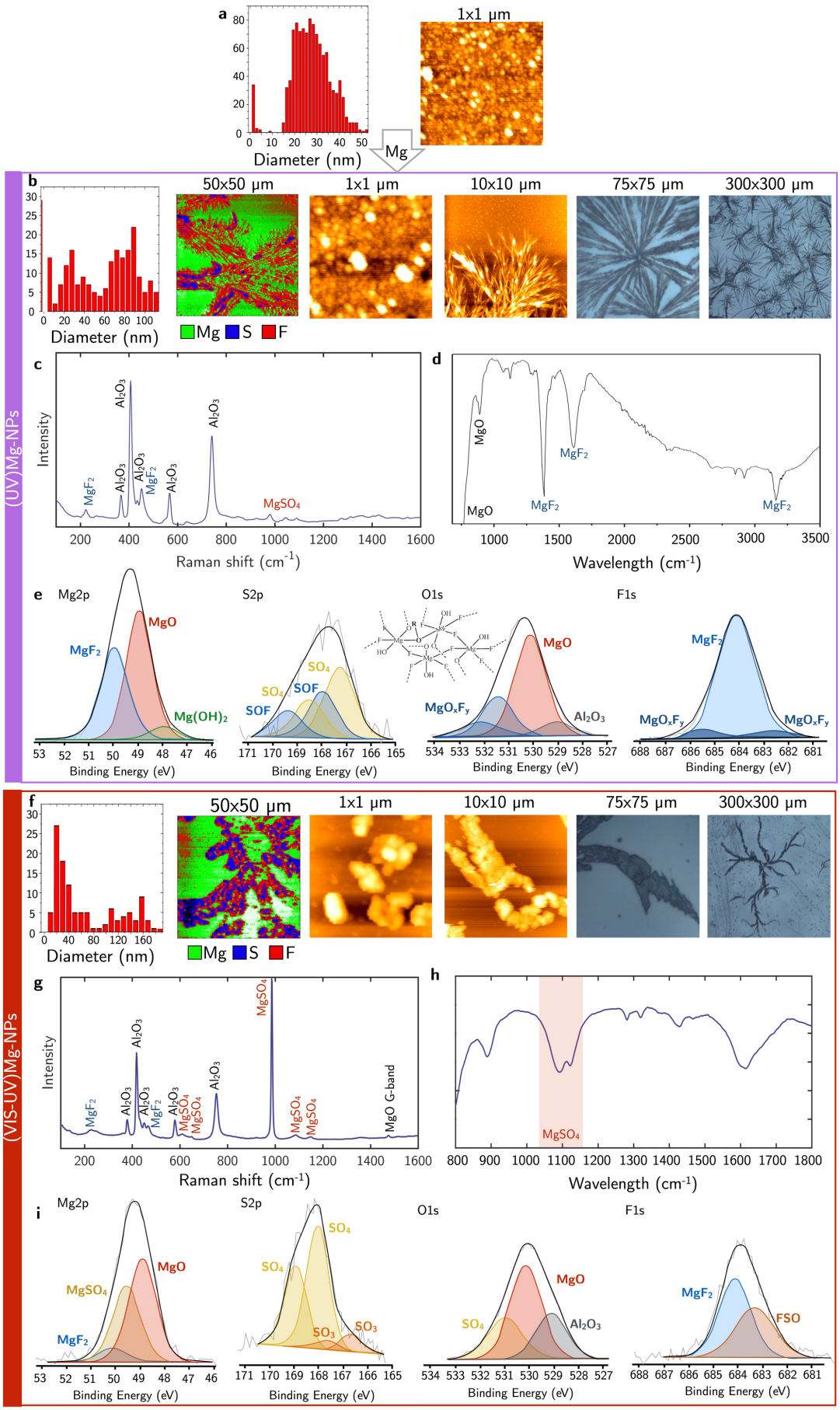
a
1x1 μm
Diameter (nm)
Mg
(UV)Mg-NPs
b
50x50 μm
1x1 μm
10x10 μm
75x75 μm
300x300 μm
Diameter (nm)
Mg S F
c
Intensity
Raman shift (cm-1)
d
MgO
MgF2
Wavelength (cm-1)
e
Mg2p
S2p
O1s
F1s
MgO
MgF2
Mg(OH)2
SO4
SOF
MgOxFy
Al2O3
FSO
Binding Energy (eV)
(VIS-UV)Mg-NPs
f
g
MgO G-band
h
i

Figure 2. Change in the surface morphology and chemical analysis of Mg NPs with UV and VIS-UV LSPRs after exposure to SF_6 contaminated air. (**a**) AFM morphology and size distribution of the Mg NPs during the first 50 seconds of Mg deposition. AFM morphology (1μm x 1μm and 10μm x 10μm), corresponding NPs size distribution and optical microscopy images (75μm x 75μm and 300μm x 300μm) of Mg NPs samples with initial LSPR in the (**b**) UV and (**f**) VIS-UV range after exposure to SF_6 contaminated air. The (50μm x 50μm) AFM phase images indicate with different colors the different probed chemical nature of the crystals (green corresponding to MgO, red corresponds to MgF_2 and blue corresponding to $MgSO_4$). **(c,g)** Raman, **(d,h)** FTIR absorbance and **(e,i)** XPS spectra of the F1s, O1s, $MgSO_4$ and Mg2p photoelectron core level of the Mg NPs samples with LSPR in the UV (top) and VIS-UV (bottom) spectral ranges. The semiquantitative XPS analysis gave for the (*UV*)Mg NPs F/Mg ~ 1.2, O/Mg ratio ~ 0.7 and a very low S/Mg <0.1whereas for the *(VIS-UV)*Mg NPs O/Mg ~ 1.8, S/Mg ~0.5 and F/Mg ~0.1

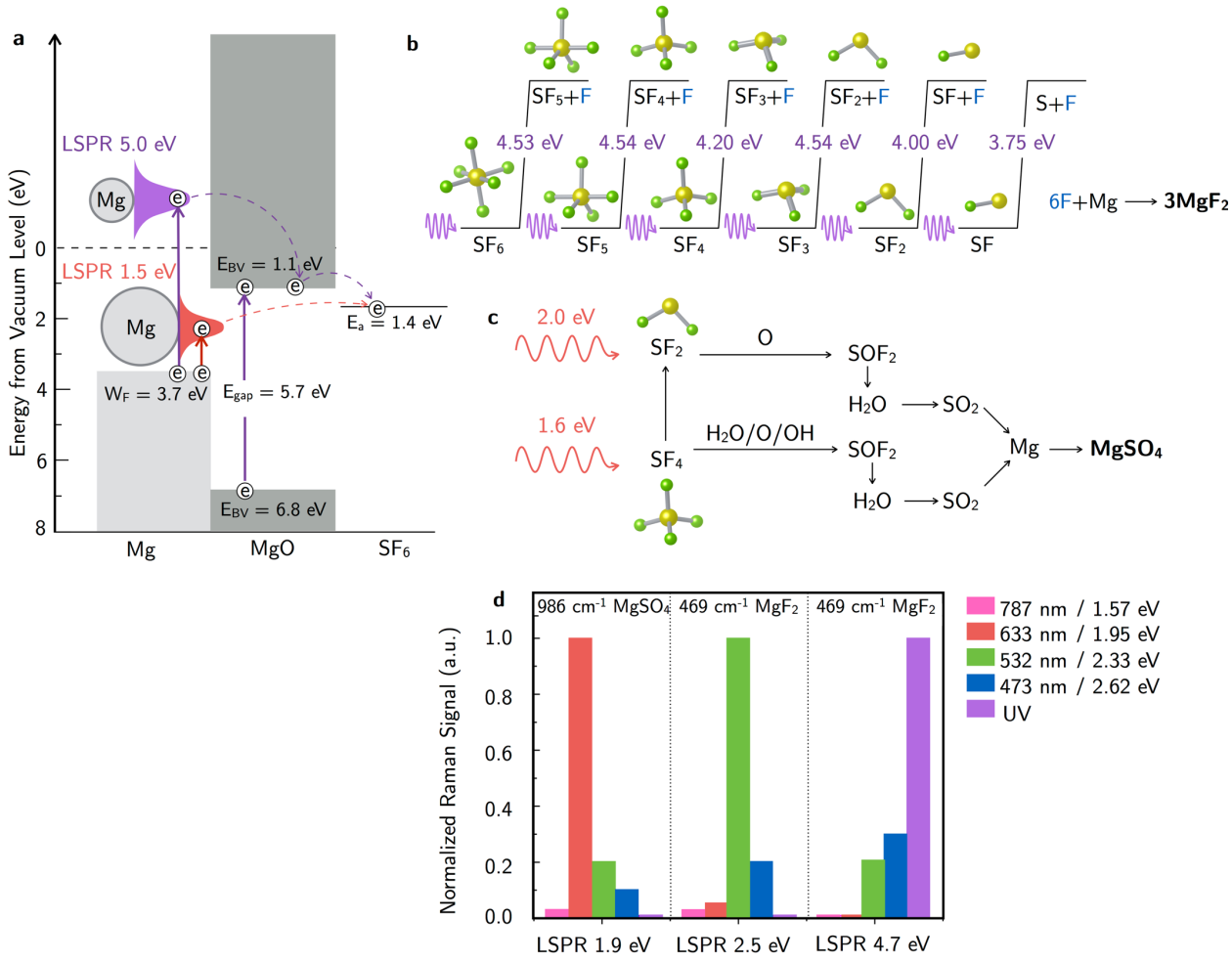

Figure 3. Mechanisms of plasmon-catalytic decomposition of SF_6 by Mg NPs and LSPR wavelength dependent product selectivity. **(a)** Energy band diagram of Mg/MgO NPs for plasmon-catalysis decomposition of SF_6. W_F refers to the Mg work function from which the LSPR level are positioned; E_{BC}, E_{BV} and E_{gap} refer, respectively, to the energy of the valence band maximum, conduction band gap minimum and of the optical bang gap of MgO. The electron affinity (E_A) energy level of the SF_6 molecule is also shown. Scheme of the plasmon-catalyzed decomposition process of SF_6 mediated by (**b**) UV plasmon (LSPR at 5 eV) and by (**c**) VIS (LSPR at 1.5 eV) plasmon**.** **(d)** Normalized Raman signal of the main by-products ($MgSO_4$ at 986 cm^{-1} and MgF_2 at 469 cm^{-1}) monitored in Mg NPs samples with LSPR energy at 1.9, 2.5 and 4.7 eV illuminated under and off resonance.

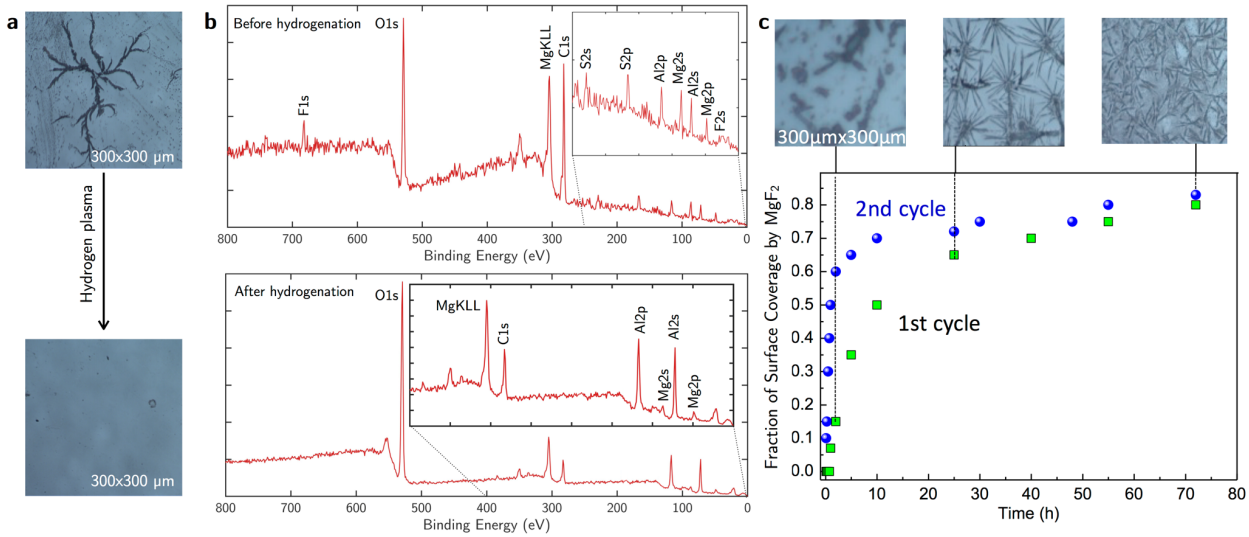

Figure 4. Mg/MgO catalyst regeneration using a hydrogen plasma treatment and its re-use. (**a**) Optical micrographies and **(b)** XPS survey spectra of the *(VIS-UV)*Mg sample before (top) and after (bottom) the hydrogen leaning process. **(c)** Kinetics of exposure of the *(UV)*Mg sample to SF_6 contaminated air before hydrogenation (1^{st} cycle) and during its re-use after the hydrogen plasma regeneration (2^{nd} cycle). The evolution of the surface coverage by MgF_2 crystals is shown which is similar for the 1^{st} and 2^{nd} cycle of Mg NPs use.

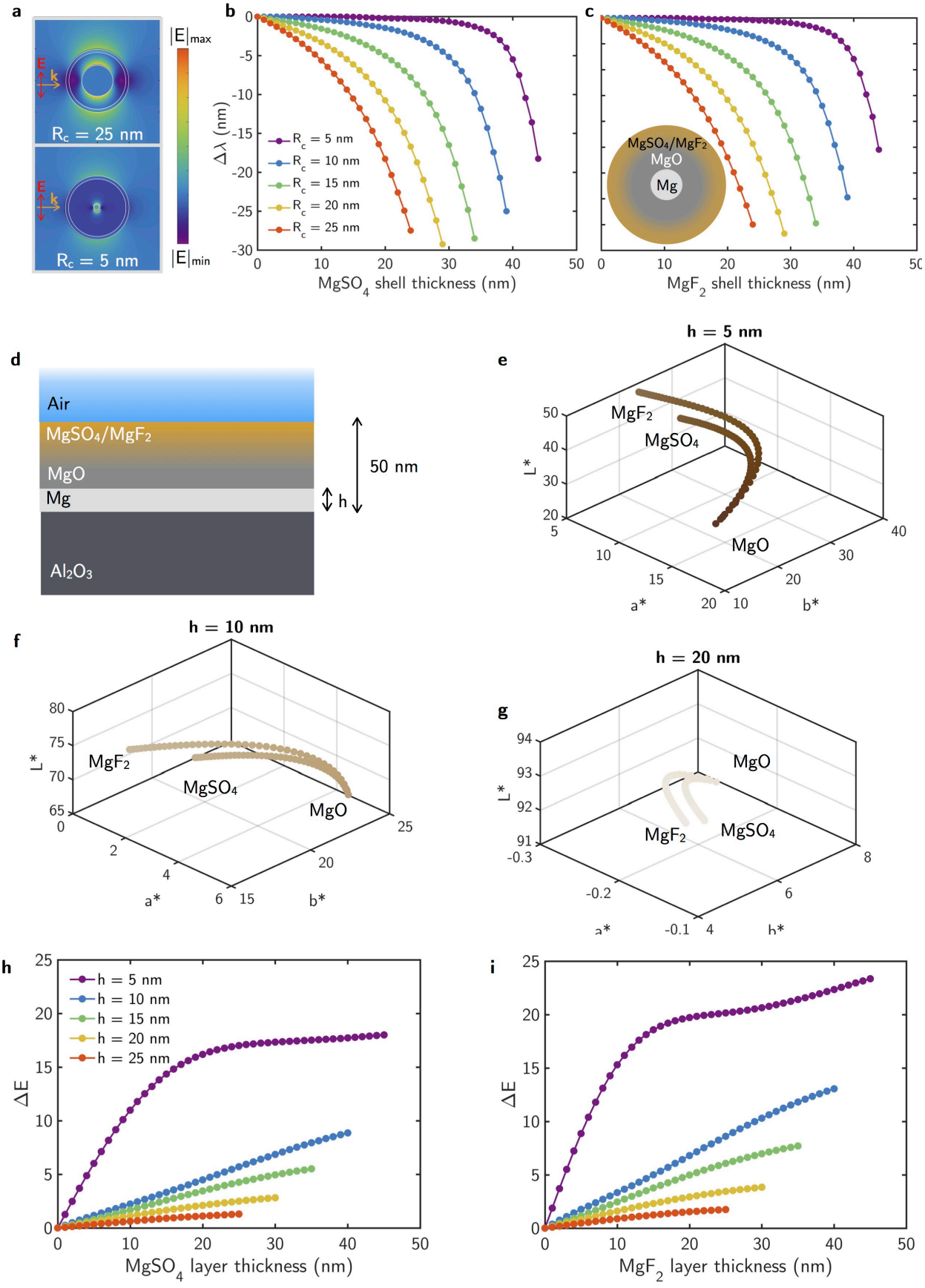
a
|E|max
|E|min
Rc = 25 nm
Rc = 5 nm
b
Δλ (nm)
Rc = 5 nm
Rc = 10 nm
Rc = 15 nm
Rc = 20 nm
Rc = 25 nm
MgSO4 shell thickness (nm)
c
MgSO4/MgF2
MgO
Mg
MgF2 shell thickness (nm)
d
Air
MgSO4/MgF2
MgO
Mg
Al2O3
50 nm
h
e
h = 5 nm
MgF2
MgSO4
MgO
L*
a*
b*
f
h = 10 nm
MgF2
MgSO4
MgO
L*
a*
b*
g
h = 20 nm
MgO
MgF2
MgSO4
L*
a*
b*
h
ΔE
h = 5 nm
h = 10 nm
h = 15 nm
h = 20 nm
h = 25 nm
MgSO4 layer thickness (nm)
i
ΔE
MgF2 layer thickness (nm)

Figure 5. Plasmonic and colorimetric sensing of the SF_6 photocatalyzation by-products. Plasmonic simulations on a Mg/MgO core shell of total radius R = 50 nm and core radius R_c. The MgO shell is converted progressively into $MgSO_4/MgF_2$ until it is completely consumed (100% $MgSO_4/MgF_2$ shell) (see inset it **c**). (**a)** Near-field map of the modulus of the local electric field for a Mg/MgO/MgF_2 multilayered sphere with R_c = 5 and 25 nm and MgF_2 shell thickness of 5 nm. With arrows are indicated incident electric field polarization, $\boldsymbol{E}$, (red) and propagation direction, $\boldsymbol{k}$, (yellow). (**b, c)** Spectral shift ($\Delta\lambda$) of the LSP dipolar resonance as the MgO shell is converted to $MgSO_4/MgF_2$ with respect to the spectral position of the 100% MgO shell. This calculation has been performed for different values of R_c while keeping the total radius fixed to R = 50 nm. (**d)** Scheme of the geometry in which the colorimetric simulations have been performed: multilayer system constituted by an infinite Al_2O_3 substrate, a Mg layer of thickness h, a layer of MgO which is converted in $MgSO_4/MgF_2$ and air as surrounding medium. The total thickness of the Mg and MgO layers have been fixed to 50 nm. (**e-g)** Color coordinates in L*a*b* space of Mg thin films with thickness (**e),** h = 5 nm, (**f)** and h = 10 nm and **(g)** h = 20 nm covered by MgO layer converted progressively into MgF_2 and $MgSO_4$. The color of each dot corresponds to the color of the film. (**h,i),** Color difference ΔE between the 100% MgO layer and the progressive conversion into (**h)** $MgSO_4$ and (**i)** MgF_2.